Journal of Zhejiang University-SCIENCE A 2026 27(6):625-639
www.jzus.zju.edu.cn; www.springer.com/journal/11582
E-mail: jzus_a@zju.edu.cn

Research Article
https://doi.org/10.1631/jzus.A2500653

Check for updates

3D printing of wet-bonded multilayer scaffolds for skin wound repair

Kangning SHEN[1,2*], Jingyi GU[3*], Ximin YUAN[4], Nian LIU[4], Yinglin WANG[3], Jiabin CAI[1,2], Yang SHI[3], Kaiyang WANG[4], Xinghua YE[2], Minghao YANG[2], Zhiyong MA[1,2✉], Zhijian XIE[3✉]

[1]*Zhejiang Key Laboratory of Industrial Solid Waste Thermal Hydrolysis Technology and Intelligent Equipment, Huzhou University, Huzhou 313000, China*
[2]*School of Engineering, Huzhou University, Huzhou 313000, China*
[3]*Stomatology Hospital, School of Stomatology, Zhejiang University School of Medicine, Zhejiang Provincial Clinical Research Center for Oral Diseases, Zhejiang Key Laboratory of Oral Biomedical, Zhejiang-Singapore International Joint Laboratory of Oral Bioengineering, Zhejiang Clinovation Pride, Hangzhou 310016, China*
[4]*State Key Laboratory of Fluid Power and Mechatronic Systems, School of Mechanical Engineering, Zhejiang University, Hangzhou 310058, China*

Abstract: The skin repair process is significantly influenced by the regulation of a dynamic mechanical microenvironment. However, traditional single-layer scaffolds face limitations, including poor mechanical compatibility and weak interfacial adhesion. These drawbacks stem from their inability to mimic the multilayer heterogeneous structure and functional synergy of natural skin. In this paper, a biomimetic skin extracellular matrix (ECM) scaffold with a layered structure bio-polycaprolactone (PCL) skin (BPS) is proposed, consisting of three layers: a surface layer (SL), a support layer (PL), and a base layer (BL). The SL consists of a 3D-printed microporous PCL structure, which simulates the epidermal barrier's antibacterial and breathable properties. The PL, a surface-modified multilayer PCL scaffold, mimics the dermal layer and provides essential mechanical support and elasticity. The BL, a hydrogel coated onto the surface of the PL, provides excellent biological properties. Genipin serves as a crosslinker, and ethylenediamine is used for amination treatment of the PCL scaffold surface. This chemical crosslinking strengthens interlayer connections, enhancing functional synergy and tripling the anti-swelling properties of the hydrogel. Additionally, it improves the wet adhesion of the scaffold to skin tissue, ensuring stable adherence to the wound surface. Compared to traditional scaffolds, this multilayer structure effectively integrates biological functions with mechanical performance, providing sustained protection and support during wound healing.

Key words: 3D printing; Biomimetic skin; Wet adhesive; Polycaprolactone (PCL) modification; Genipin

1 Introduction

As the primary barrier against mechanical damage, skin repair critically depends on the regulation of a dynamic mechanical microenvironment (Trichet et al., 2012; Hunter-Featherstone et al., 2021). While conventional scaffolds provide basic protection (Drobnik and Stebel, 2017), they fail to replicate the synergistic interplay between the biomechanical properties and biological functions of natural skin, limiting healing efficacy (Boateng and Catanzano, 2015). Although structural optimization of single-layer scaffolds has enhanced mechanical adaptability (Dhandayuthapani et al., 2011; O'Brien, 2011), the inherent homogeneity of these designs fundamentally contrasts with the mechanical heterogeneity and functional synergy of the epidermis-dermis-subcutaneous tissue triad in human skin. Consequently, these scaffolds exhibit weak adhesion, poor biocompatibility, and mechanical mismatch (Obagi et al., 2019; Barros Almeida et al., 2021; Maaz Arif et al., 2021). Recently, biomimetic multilayer architectures have emerged as a breakthrough strategy (Yao et al., 2025). Similar multilayer or multi-region biomimetic designs have also been successfully applied in cartilage tissue engineering (Chen Y et al., 2025) and in dermal scaffolds fabricated by digital light processing (DLP) 3D printing (Han et al., 2025),

✉ Zhiyong MA, 02641@zjhu.edu.cn
Zhijian XIE, xzj66@zju.edu.cn
* The two authors contributed equally to this work
Zhiyong MA, https://orcid.org/0000-0002-3712-1397
Zhijian XIE, https://orcid.org/0000-0003-0122-0948

Received Dec. 15, 2025; Revision accepted Jan. 13, 2026;
Crosschecked Apr. 8, 2026; Online first June 5, 2026

further supporting the rationale of our stratified approach. Building on this concept, a tri-layered biomimetic skin repair extracellular matrix (ECM) scaffold bio-polycaprolactone (PCL) skin (BPS) was developed, integrating structural support and bioactivity by replicating the hierarchical functions of epidermal, dermal, and subcutaneous tissues (Brohem et al., 2011). The multilayer ECM scaffold features functional biomimicry: The surface layer (SL) is a multilayer composite PCL porous film mimicking the epidermal antibacterial barrier and breathability (Barbu et al., 2021). The support layer (PL) is a PCL scaffold replicating dermal mechanical properties and structural support (Arif et al., 2022), with surface-aminated PCL enhancing interfacial crosslinking with the base layer (BL) to resist horizontal swelling and delamination. The BL is a gelatin hydrogel modified to address two limitations of natural gelatin—rapid degradation mismatched with skin repair cycles (van den Bosch and Gielens, 2003; Gronbeck and Feng, 2023) and a mechanical modulus significantly lower than that of human subcutaneous tissue (Yazdi and Baqersad, 2022). A salt-ion shielding effect (Huo et al., 2025) was used to weaken intermolecular hydrogen bonds, enabling the formation of free single-chain gelatin molecules. Subsequent mechanical agitation produced a highly entangled gelatin hydrogel network with biomimetic mechanical adaptability and controlled degradation (Nian et al., 2022) while maintaining cytocompatibility comparable to subcutaneous tissue. Genipin, a natural crosslinker, was used to covalently crosslink amino groups on the scaffold with those on moist wound surfaces (Meng and Shen, 2018; Yu et al., 2021), ensuring stable scaffold–wound interfacial integration.

Systematic evaluations of the mechanical behavior, antibacterial activity, and cellular responses of BPS demonstrated superior biomechanical similarity to human skin, excellent biocompatibility, unidirectional antibacterial properties, and degradation kinetics aligned with skin repair timelines. The scaffold also showed effective wet adhesion. Animal experiments further confirmed enhanced repair efficacy compared to single-layer scaffolds and controls. This study innovatively establishes a multifunctional repair system integrating mechanical adaptation, antibacterial regulation, biological activity, and wet adhesion. It offers a modular design paradigm for biomimetic materials in tissue engineering and a versatile scaffold platform for skin repair ECM (Zhao et al., 2025).

2 Experimental

Materials: Gelatin (type B, bovine) was purchased from Sigma-Aldrich, Germany. Phosphate-buffered saline (PBS) was obtained from Meilum, China. Glycerol, sodium citrate (SC) (dihydrate), genipin, ethylenediamine (EDA), and sodium hydroxide (NaOH) were acquired from Shanghai Aladdin Biochemical Technology Co., Ltd., China. PCL and deionized water (DI water) were supplied by Zhejiang University, China. All reagents were analytical grade and used without further purification.

Preparation of BL hydrogel: Gelatin granules were dissolved in PBS at 50 °C, forming a 100 g/L gelatin solution. Genipin (5 g/L) was then added and stirred continuously until fully dissolved. SC (10 g/L) was introduced and stirred at 800 r/min for 5 min to enhance molecular entanglement. Finally, glycerol (2.5, 5.0, or 7.5 g/L) was added to produce hydrogel precursor solutions designated as low (LG), medium (MG), and high (HG) glycerol groups. Solutions were stored at 37 °C.

Preparation of SL and PL: A customized melt near-field electrostatic direct-writing system (EFL-BP6601, Suzhou Institute of Intelligent Manufacturing, China) was used for printing. PCL pellets were loaded into the printing barrel. For SL-layer nonwoven printing, the barrel was heated to 100 °C for 15 min; the nozzle diameter was 150 μm; the nozzle-to-substrate distance was 5 mm; the extrusion air pressure was 30 kPa; the voltage was 8 kV; and the substrate speed was 150 mm/min. After printing, the nonwoven mat was heated briefly at 85 °C and stacked to form a three-layer SL structure. The PL layer was directly deposited onto the SL. In this step, the barrel was heated to 105 °C; the nozzle-to-substrate distance was 1.8 mm; the voltage was 4.2 kV. After printing, samples were designated as the PCL-p group, and an outer frame was printed using fused deposition modeling (FDM) to facilitate collection. The PCL-p scaffolds were immersed in 400 g/L NaOH solution for 1 h at room temperature, rinsed three times with DI water, and designated as the PCL-h group. Finally, PCL-h scaffolds were immersed in 10% (volume fraction) EDA solution at room temperature for 30 min, thoroughly rinsed with DI water, air-dried, and labeled as the PCL-a group.

Fabrication of the BPS biomimetic skin: A hollow rectangular mold (15 mm×35 mm) was printed via

FDM. The amino-functionalized PCL-a scaffold was positioned centrally within the mold cavity. Subsequently, 2 mL preheated BL-layer solution was slowly added to completely cover the scaffold. The mold was held at room temperature for 15 min to facilitate gelation and minimize in-plane shrinkage. The composite hydrogel and mold were freeze-dried at −50 ℃ under vacuum (<10 Pa) for 24 h. The finished BPS was removed and stored under vacuum.

Scanning electron microscopy (SEM): Freeze-dried samples were sputter-coated with gold. SEM (Oxford Instruments, UK) was conducted at 15 kV to analyze the internal hydrogel morphology, surface topography of PL/SL, and energy dispersive X-ray spectroscopy (EDS) elemental distribution of the modified PL surfaces.

Fourier transform infrared spectroscopy (FT-IR): Freeze-dried samples were analyzed using a Nicolet NEXUS-470 spectrometer (Thermo Fisher Scientific, USA) at 4 cm^{-1} resolution with 32 cumulative scans.

X-ray photoelectron spectroscopy (XPS): Samples mounted on metal stubs were Au-Pd-coated (Desc II, Denton Vacuum, USA). Surface chemistry was analyzed via XPS (Escalab 250Xi, Thermo Fisher Scientific, USA).

X-ray diffraction (XRD): XRD was performed using a Gemini A OHra diffractometer to investigate crystal structural changes in PL.

Mechanical testing: LG/MG/HG hydrogels were molded into dumbbell-shaped specimens (20.0 mm×4.0 mm×1.5 mm). Tensile tests (GB/T 1040.3-2006) (AQSIQ, 2006) were performed using a UTM2102 universal testing machine at 5 mm/min. Melt electrowriting (MEW)-printed PL (PCL-p, PCL-h, and PCL-a) and BPS composites were tested for elastic modulus under identical conditions.

Adhesion testing: Porcine skin (10 mm×10 mm squares) was coated with BL solution and attached to 3D-printed tensile plates secured with adhesive tape. Samples were immersed in PBS to simulate wet conditions until fully crosslinked. Interfacial toughness was measured via T-peel testing (ASTM, 2024) using UTM2102 at 5 mm/min. Interfacial toughness was calculated as the plateau force divided by twice the sample width (Guo et al., 2023).

Degradation experiment: Hydrogels were prepared according to the ASTM method (ASTM, 2016). Samples were cut into suitable shapes, weighed (W_0), and incubated in 25 mL PBS (pH 7.4) at 37 ℃ for 15 d. Every three days, three independent samples were removed, freeze-dried, and weighed (W_t). Degradation was calculated as the percentage weight loss (ΔW) using the following equation (Liu et al., 2020):

$$\Delta W = (W_0 - W_t)/W_0. \tag{1}$$

Swelling experiment: Hydrogels were immersed in PBS at 37 ℃ for 24 h to measure their swollen mass (W_s). Subsequently, the samples were freeze-dried to obtain the dry mass (W_d). The swelling ratio (R_S) was calculated using:

$$R_S = (W_s - W_d)/W_s. \tag{2}$$

Horizontal swelling experiment: Custom molds (15 mm×10 mm×2 mm) were 3D-printed to prepare control group (CG) and BPS samples. Samples were freeze-dried under vacuum. The initial horizontal length and width were recorded (W_{x_1}, W_{x_2}). The hydrogels were immersed in PBS at 37 ℃ for 24 h, after which their horizontal dimensions (W_{y_1}, W_{y_2}) were remeasured. The horizontal swelling ratio (R_{HS}) was calculated as:

$$R_{HS} = (W_y - W_x)/W_x. \tag{3}$$

BL and PL interface mechanical testing: PCL-p, PCL-h, and PCL-a scaffolds with 300 and 500 μm fibers were vertically inserted into BL hydrogels. After crosslinking, test specimens were prepared. Custom 3D-printed testing molds (Fig. S1 of the electronic supplementary materials (ESM)) were used, and interface mechanical testing was conducted using a UTM2102 universal testing machine at a tensile speed of 5 mm/min.

Air permeability test: A 50 mm×50 mm SL sample was prepared, and gas permeability was measured using the pressure differential method. Measurements were performed with a PAPT-B02 membrane air permeability tester, using air as the test gas.

Cell culture: Fibroblasts were cultured in Dulbecco's modified eagle medium (DMEM) (HyClone, USA) supplemented with 10% (volume fraction) fetal bovine serum (10091-148, Gibco, USA) at 37 ℃ under 5% CO_2.

Cell viability and proliferation assay: Cell proliferation was evaluated using a CCK-8 kit (CK001,

Lablead, China). Cells (3×10^4 per well) were seeded in Transwell-24 plates (NEST Biotechnology Co. Ltd., China), with test membranes placed in the upper chambers. After 1, 3, 5, and 7 d, absorbance at 450 nm was measured following a 2 h incubation with 10% CCK-8 reagent. For live/dead staining, cells cultured for 5 d were stained using a Calcein-AM/PI kit (BB-4126, Bestbio, China) for 40 min and imaged using an inverted fluorescence microscope (BZ-X800, KEYENCE, Japan).

Bacterial isolation assay: Membranes were immersed in 24-well plates containing 1 mL bacterial suspension (1×10^8 CFU/mL of *Escherichia coli* or *Staphylococcus aureus*, where CFU indicates the colony forming unit) and incubated at 37 ℃ with shaking for 2 h. After washing with PBS, samples were fixed with 4% glutaraldehyde (4 ℃ overnight), dehydrated through graded ethanol solutions (30%–100%, 15 min per step), and observed by SEM.

Quantitative polymerase chain reaction (qPCR): total RNA was extracted using TRIzol (15596, Invitrogen, USA) and reverse-transcribed into cDNA using PrimeScript RT Master Mix (RR036, Takara, Japan). qPCR was performed with TB Green Premix Ex Taq (RR420A, Takara, Japan) on a CFX384 Real-Time Polymerase Chain Reaction System (RT-PCR) (Bio-Rad, USA) under the following conditions: 95 ℃ for 30 s, followed by 40 cycles of 95 ℃ for 5 s and 60 ℃ for 32 s. Glyceraldehyde-3-phosphate dehydrogenase (GAPDH) was used as the internal control. Relative mRNA expression was calculated using the comparative threshold method (Table S1 of the ESM).

Immunofluorescence staining: Cells cultured on membranes for 3 d were incubated with a primary antibody against vinculin (VCL) (400:1, 26520-1-AP, Proteintech) at 4 ℃ overnight, followed by incubation with a secondary antibody (400:1, Abcam). Fluorescence signals were visualized using a fluorescence microscope (BZ-X800, KEYENCE, Japan).

Rat skin defect model: Full-thickness skin defects (1.5 cm in diameter) were created on Sprague–Dawley rats, with approval from the Ethics Committee for Animal Research at Zhejiang University, and conducted in accordance with the guide for the care and use of laboratory animals. Rats were anesthetized with sodium pentobarbital (10 g/L, 0.4 mL per 100 g body weight) and divided into control (untreated) and experimental (membrane-implanted) groups. Three rats per group were sacrificed on days 4, 7, and 14 post-surgery for wound observation. On day 4, undegraded materials were removed, and wound images were captured. Subsequently, wound tissues and adjacent normal skin were harvested for histological analysis.

Histological evaluation: Tissues were fixed in 4% paraformaldehyde for 24 h, paraffin-embedded, sectioned (5 μm), and stained with hematoxylin and eosin staining (H&E) and Masson's trichrome. CD31 immunofluorescence and VCL immunohistochemistry were performed to assess angiogenesis and cell adhesion. The wound closure rate, collagen deposition, and CD31/VCL-positive areas were semi-quantified using ImageJ (NIH, USA).

Statistical analysis: Data are presented as mean± SD (standard deviation). Intergroup differences were analyzed using one-way ANOVA (SPSS 26.0), with $P<0.05$ considered statistically significant.

3 Results and discussion

3.1 Design and fabrication of the BPS

The BPS consists of three components: the BL, PL, and SL (Fig. 1). To ensure the efficacy of the biomimetic skin in repairing skin defects, BPS should exhibit excellent biocompatibility and mechanical properties matching human skin. The gelatin hydrogel demonstrates favorable elasticity and biocompatibility, and its abundant collagen closely resembles the skin composition (Tang et al., 2021). By incorporating genipin to form a gelatin–genipin (Gel-GN) hydrogel, the BL retains favorable biological properties. Additionally, genipin's nucleophilic ring-opening reaction promotes crosslinking between amino groups (Meng and Shen, 2018), ensuring adhesion of biomimetic skin in wet environments. However, the low mechanical strength of gelatin hydrogels limits their application in tissue repair. Studies indicate that adding high-strength fibrous materials to hydrogels can significantly enhance their mechanical properties (Agrawal et al., 2013; Chen YW et al., 2025). Therefore, a multilayer PCL framework printed via MEW technology was embedded into gelatin as a mechanical core to provide structural support and mechanical stability.

Based on this, an innovative Gel-PCL preparation process was developed to achieve long-lasting and stable chemical crosslinking between the PL and BL.

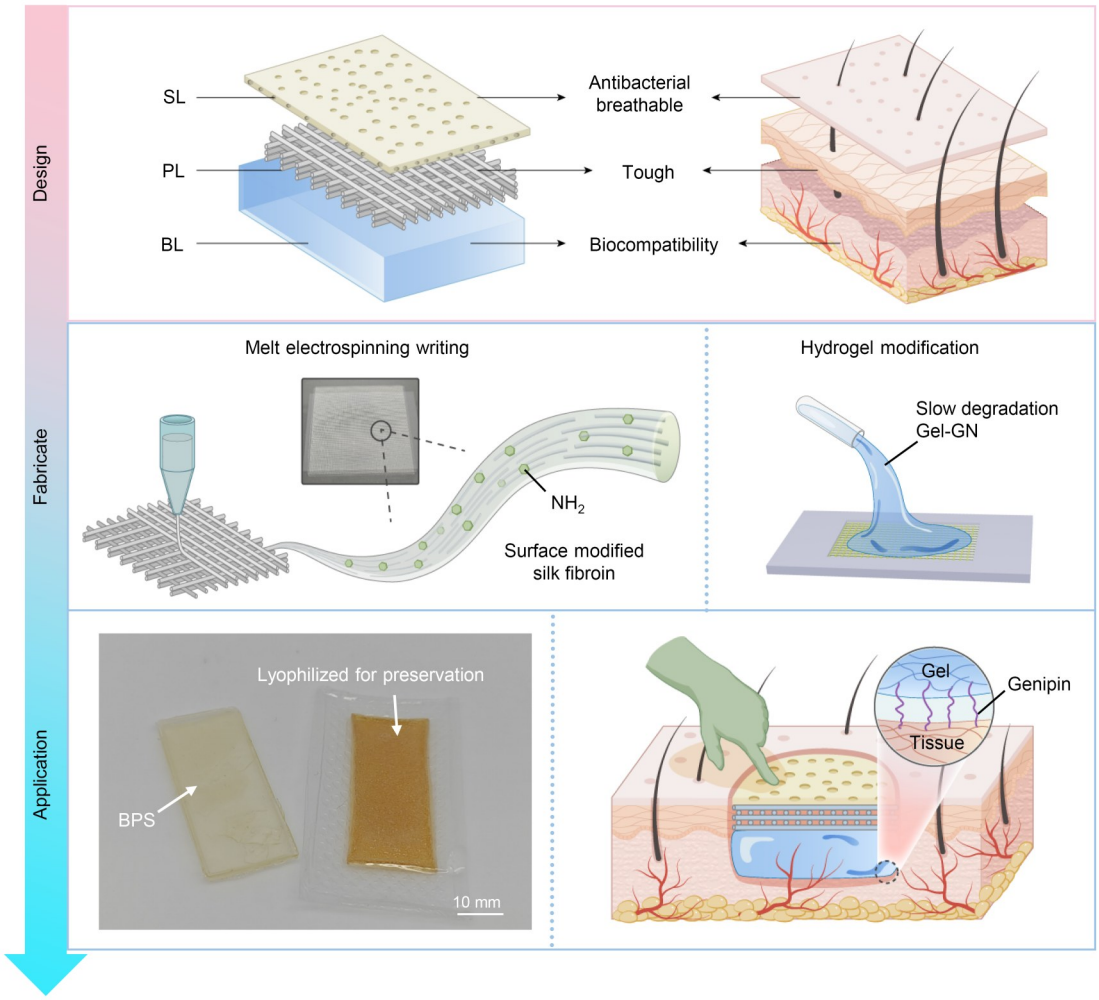

Fig. 1 Schematic illustration of BPS design and fabrication

First, PCL molecular chains are opened through saponification to introduce carboxyl groups (–COOH). Subsequently, amino groups (–NH_2) are generated via condensation reactions between carboxyl groups and ethylenediamine. Genipin's nucleophilic ring-opening reaction in the hydrogel then promotes crosslinking between amino groups, ultimately forming a stable bio-PCL structure. Finally, using MEW technology and the "whip effect" (Robinson et al., 2019), a porous PCL nonwoven SL with an average pore size of 20 μm is fabricated. Three layers of this membrane are superimposed, resulting in a surface film with excellent antibacterial and breathable properties. Multilayer integration yields the final BPS biomimetic skin. All materials selected are biodegradable and FDA-approved, demonstrating outstanding application potential.

3.2 Physicochemical properties of the base layer

Gelatin and genipin were thoroughly mixed to prepare the Gel-GN hydrogel BL, with its crosslinking process proceeding slowly (Fig. 2a). Traditional Gel-GN hydrogels exhibit poor mechanical properties, often rupturing under external forces. Their modulus significantly differs from that of skin tissue, compromising recovery. Glycerol, an internal plasticizer, physically interacts with materials without forming covalent bonds, enhancing plasticity and fluidity (Patel et al., 2013). To improve the mechanical performance, glycerol is incorporated and uniformly dispersed into the Gel-GN solution. The cross-sectional morphology of freeze-dried Gel-GN films with variable glycerol concentrations was observed via SEM (Fig. 2c). The analysis revealed phase separation of glycerol within

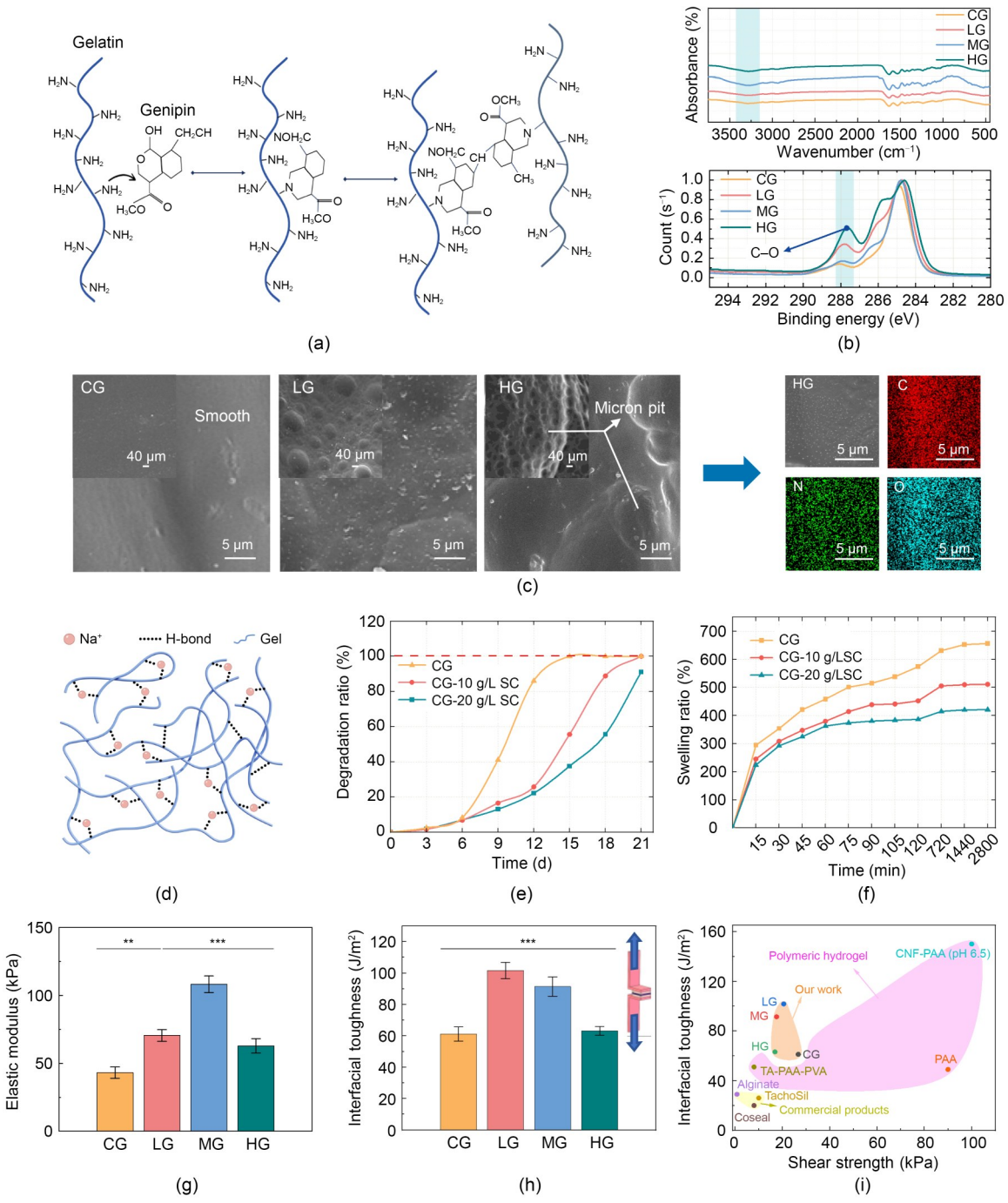

Fig. 2 Preparation mechanism and characterization of the base layer: (a) Gel-GN crosslinking mechanism; (b) XPS and FT-IR spectra; (c) SEM and EDS characterization of Gel-GN films; (d) cation shielding mechanism diagram; (e) gel degradation with increased entanglement; (f) gel swelling with increased entanglement; (g) elastic modulus of BL with varying glycerol content; (h) interfacial toughness of the BL; (i) SEM surface scan of Gel-GN films (g and h: mean±SD, ** P<0.01, *** P<0.001, n=3). PAA: polyacrylic acid; PVA: polyvinyl alcohol; CNF: cellulose nanofiber; TA: tannic acid

the Gel-GN solution and formation of numerous microcavities. These microcavities effectively dissipate stress, thereby enhancing the mechanical properties of the Gel-GN films.

To identify the optimal glycerol concentration, Gel-GN solutions containing 2.5, 5.0, and 7.5 g/L glycerol (LG, MG, and HG) and a CG were prepared. Chemical analysis (Fig. 2b) confirmed the regulatory

role of glycerol in genipin crosslinking within the Gel-GN solution. FT-IR spectra showed a $–NH_2$ vibration peak at 3300 cm^{-1} and an amide bond absorption peak near 1643 cm^{-1}. Gradual addition of glycerol up to 5.0 g/L resulted in the narrowest full width at half maximum (FWHM). Higher glycerol concentrations reduced the crosslinking density. The absorption peak at 3300 cm^{-1}, smaller and flatter than that of pure gelatin, indicated crosslinking of $–NH_2$ groups. Concurrently, the amide bond absorption peak at 1643 cm^{-1} showed the narrowest FWHM at a glycerol concentration of 5.0 g/L. Further XPS analysis of C–O bonds near the 288 eV peak (calibrated against carbon at 285 eV) revealed the lowest C–O bond signal in the MG group. This confirmed increased genipin–gelatin reactions and loss of carboxyl groups, aligning with FT-IR results and validating glycerol's regulatory effect on Gel-GN crosslinking.

Human skin typically requires 2–4 weeks for complete healing after severe trauma. However, gelatin-based materials degrade rapidly (in approximately 10 d), mismatching tissue regeneration timelines. Studies suggest that hydrogel degradation can be controlled by optimizing molecular chain entanglement (Li and Gong, 2024). Leveraging this, hydrogel molecular chain entanglement was adjusted to regulate degradation. SC, selected via the Hofmeister effect for its biocompatibility, weakens gelatin intermolecular hydrogen bonds through salt-ion shielding (Fig. 2d) without inducing protein denaturation, forming free single chains. Mechanical agitation then reconstructs these into a highly entangled network, with entanglement quantified by rheology (Nian et al., 2022) (Fig. S2 of the ESM).

To demonstrate SC's effect, three groups (CG, CG-10 g/L SC, and CG-20 g/L SC) were evaluated for degradation and swelling (Figs. 2e and 2f). The data showed that SC significantly enhanced the anti-swelling capability and degradation stability of the Gel-GN composites. Although the CG-20 g/L SC group exhibited stronger anti-swelling properties, its degradation rate was too slow for human skin repair cycles (Singer and Clark, 1999). Thus, a 10 g/L SC concentration was selected to construct the BL structure.

Mechanical testing revealed glycerol's dual regulatory effect on BL behavior: moderate glycerol increased the hydrogel elastic modulus to 108 kPa (Fig. 2g) and fracture stress to 882.36 kPa (Fig. S3 of the ESM), meeting subcutaneous tissue mechanical demands. Excessive glycerol, however, suppressed genipin crosslinking and reduced overall performance. Porcine skin was selected as a model for adhesion evaluation due to its mechanical robustness and similarity to human skin. Gel-GN films crosslinked with porcine skin in PBS exhibited an interfacial toughness of 101.72 J/m^2 (Fig. 2h) and a shear strength of 26.69 kPa (Fig. S4 of the ESM). These values surpassed those of commercial bioadhesives and reported degradable hydrogels (Guo et al., 2023; Park et al., 2023; Zhang et al., 2023; Wu et al., 2024) (Fig. 2i). Although glycerol slightly weakened the interfacial strength, the CG group failed prematurely due to insufficient mechanical strength, resulting in lower interfacial toughness compared to the MG group. Considering mechanical compatibility and interfacial stability, the MG formulation was ultimately selected for BL fabrication.

3.3 3D printing of the support and surface layers

Three-dimensional random networks were fabricated using the "whipping effect" with non-directional fiber deposition under high voltage via MEW technology (Fig. 3a). These networks were thermally fused to form porous membranes, with three superimposed layers serving as the SL. Ultramicropores in the SL provided excellent bacterial retention and breathability. A highly aligned PL fiber bundle was printed on the SL surface to enhance structural support and mechanical performance, with an optimized fiber diameter of 15 μm (Liu et al., 2025). To achieve a low-porosity SL, the relationship between printing speed and porosity under different air pressures was systematically investigated, resulting in multilayer nonwoven structures with optimized pore sizes of approximately 20 μm (Fig. 3b). In the hierarchical design of BPS, the interface stability between the PL and BL critically affects mechanical force transmission and functional integration. Although traditional mechanical interlocking strategies allow preliminary bonding (Zussman et al., 2018), interfacial slippage frequently leads to delamination or mechanical failure. To address this, a covalently crosslinked PCL-hydrogel interface was developed through surface chemical modification. Amino groups were grafted onto PL surfaces to establish covalent bonds with the genipin crosslinked BL. PCL surface modification was performed via a two-step process (Fig. 3c). Prefabricated PL-SL bilayer scaffolds were first etched with 400 g/L NaOH solution to hydrolyze

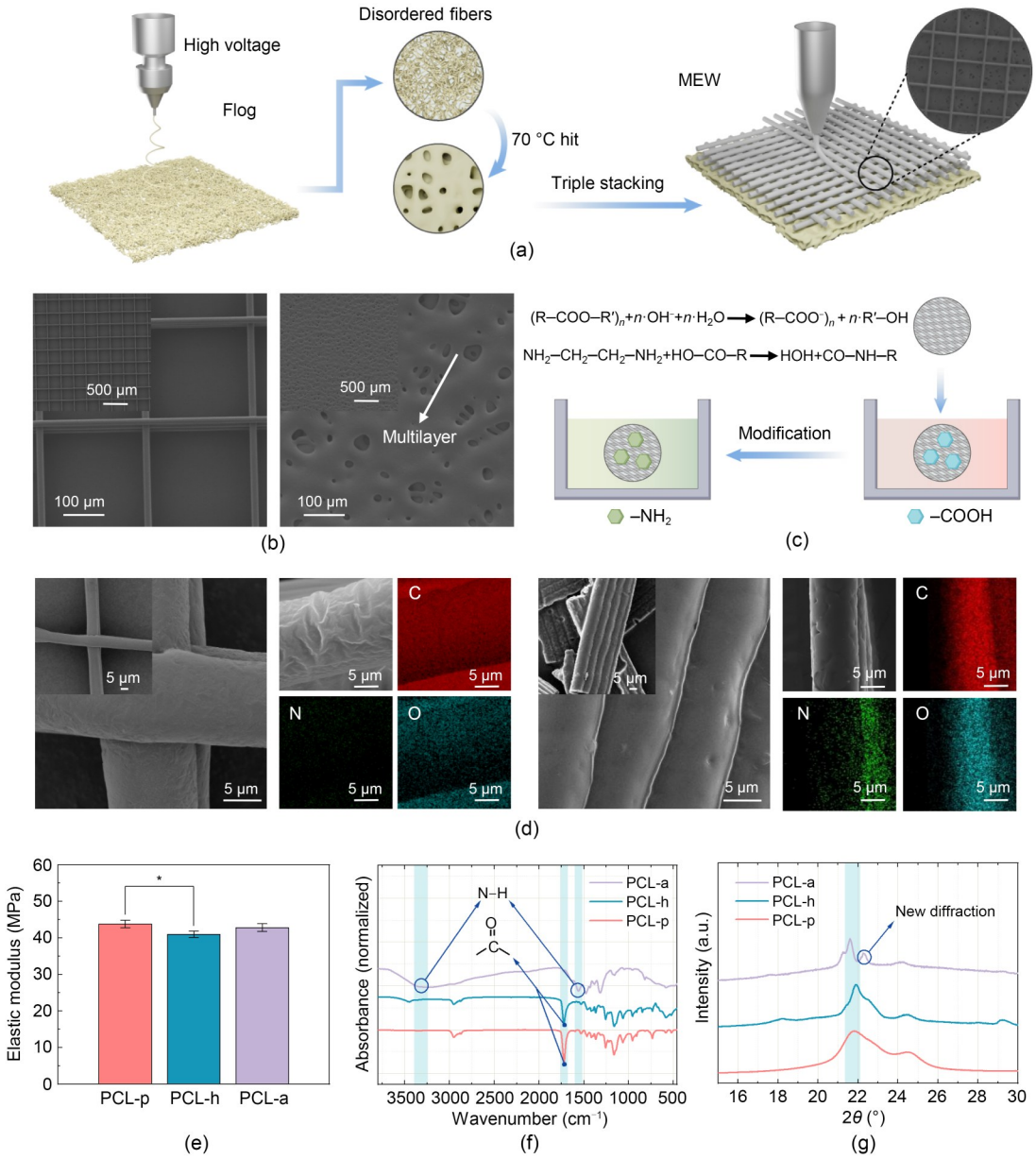

Fig. 3 Preparation and characterization of the SL and PL layers: (a) schematic diagram of the preparation process of the SL and PL; (b) SEM morphology of SL and PL; (c) schematic diagram of surface modification of PL; (d) SEM and EDS analysis of modified PL; (e) elastic modulus of modified PL (mean±SD, * P<0.05, n=3); (f) FT-IR spectrum of modified PL; (g) XRD pattern of modified PL

ester bonds, generating reactive carboxyl (–COOH) and hydroxyl (–OH) groups. After rinsing with DI water, amino modification was carried out using 10% (volume fraction) EDA solution (Zhou et al., 2005). Three experimental groups were prepared: pristine PCL (PCL-p), NaOH-treated PCL (PCL-h), and aminated PCL (PCL-a). SEM analysis revealed smoother surfaces in the PCL-a group after EDA treatment, preserving the 3D network topology. Elemental mapping demonstrated significantly increased nitrogen signals in the PCL-a group (Fig. 3d), confirming successful amino grafting. FT-IR spectroscopy (Fig. 3f) further verified chemical modifications: the characteristic carbonyl (C=O) peak at 1727 cm^{-1} remained in the PCL-h group but weakened in the PCL-a group, with new absorption peaks at 1625 and 3300 cm^{-1}. XRD analysis (Fig. 3g) showed lattice distortion characteristic peaks at 21.4° and 23.7° in the PCL-a group, induced by

amino modification, consistent with FT-IR results. Tensile testing (Fig. 3e) confirmed that PCL surface modification preserved mechanical integrity while imparting chemical activity.

3.4 BPS hydrogel membranes

In this study, we successfully constructed aminated PCL fibers (PCL-a scaffolds) whose surface amino groups could crosslink with genipin (Fig. S6 of the ESM). The scaffolds were embedded into 3D-printed customized hollow molds, followed by uniform spraying of Gel-GN precursor solution and incubation at room temperature. After the hydrogel solution completely filled the mold through self-levelling, vacuum freeze-drying terminated the crosslinking process, ultimately forming BPS hydrogel membranes (Fig. 4a). Interface shear testing demonstrated that compared with the unmodified PCL-p/PCL-h groups, the PCL-a group showed a significantly enhanced anti-slippage capability at fiber-hydrogel interfaces (Fig. 4d). Additionally, the elastic modulus of BPS reached 5.11 MPa (Fig. 4c), fully covering the mechanical spectrum of human skin (Oomens et al., 2017). Traditional freeze-dried hydrogels typically undergo intense isotropic swelling during rehydration, causing potential mechanical damage to wounds (Li and Gong, 2024). Here, the anisotropic grid topology of PL scaffolds effectively suppressed horizontal swelling: the orthogonal grid structure limited the transverse swelling ratio of BPS to 6.0%±1.6% while maintaining the longitudinal swelling ratio at 9.0%±2.5% (Fig. 4b).

To evaluate the adaptability and integration capacity of BPS for skin wounds, we observed its physical matching and adhesive behavior in a porcine ex

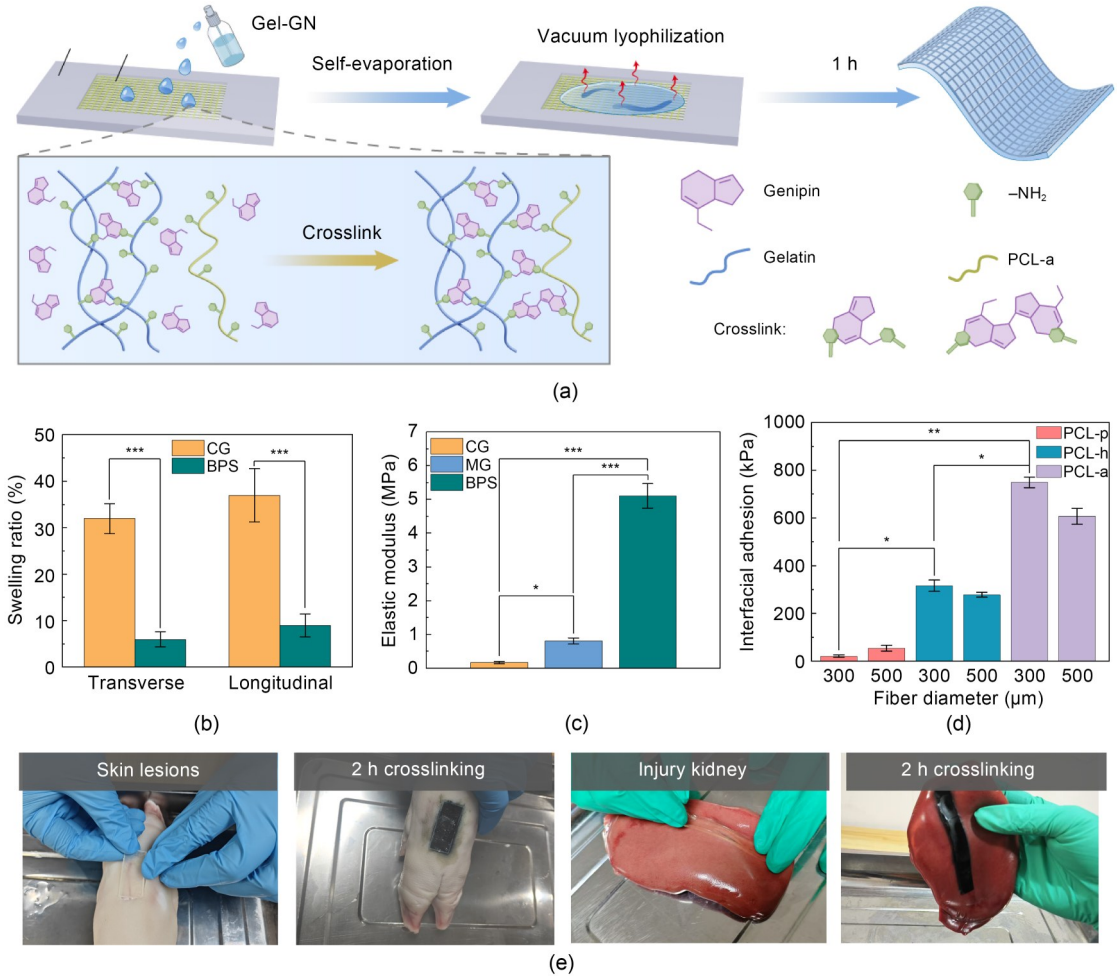

Fig. 4 Preparation and characterization of BPS hydrogel films: (a) schematic diagram of the BPS preparation process; (b) longitudinal and transverse swelling rates of BPS; (c) comparison of mechanical properties of BPS; (d) interfacial mechanics of BL and PL; (e) ex vivo tissue application of BPS (b–d: mean±SD, * P<0.05, ** P<0.01, *** P<0.001, n=3)

vivo tissue model. The BPS precisely conformed to full-thickness skin defects and formed stable adhesion to the wound edge tissue through genipin-mediated interfacial covalent crosslinking (Fig. 4e). The BPS also showed good conformability and adhesive performance in a simulated linear incision closure scenario, indicating its ability to adapt to wounds of different geometric shapes.

3.5 Experiments on different cell components

The designed BL hydrogel should exhibit excellent biocompatibility and low cytotoxicity. Live/dead cell staining and CCK-8 assays were performed to evaluate the clinical applicability of BL materials (Pan et al., 2023). Multiple control groups were established, including PCL-p, PCL-h, and PCL-a, to systematically compare material properties, with the aim of verifying the fundamental biosafety of the material system at each stage and providing a comparative basis for the overall performance of the subsequent BPS. Using a pure PCL group as a control, live/dead staining after 3 d coculture (Fig. 5b) showed normal cell morphology in the modified PCL and BPS groups, with significant proliferation observed in all groups. CCK-8 analysis revealed no significant differences among the groups (Fig. 5a). These results collectively demonstrate the excellent biocompatibility of BPS materials for biomedical applications.

As a skin repair scaffold, the SL was biomimetically designed with pore structures resembling the skin epidermal layer. Multilayer, densely stacked PCL nonwoven fabric effectively prevented bacterial invasion, demonstrating robust antibacterial performance and breathability (Fig. S5 of the ESM) to both prevent and treat wound infections (Peng et al., 2022). To evaluate the antibacterial efficacy of the SL, in vitro antimicrobial tests were conducted to assess its inhibitory effects against *E. coli* and *S. aureus* (common wound pathogens). SEM observations (Fig. 5c) revealed substantial bacterial adhesion on membrane materials lacking dense porous layers. The dense layer significantly reduced the bacterial penetration, dramatically decreasing the inner-layer bacterial colonization.

Effective adhesion properties enhance initial stability and promote cell attachment and growth (Guarino et al., 2007). RT-PCR results showed that, compared with other groups, BPS significantly upregulated the expression of Col I, VCL, Fn1, and ITGB, which are key mediators of ECM remodeling and cell–matrix adhesion, whereas no significant differences were observed in the levels of α-SMA and Ki67 markers of myofibroblast differentiation and cell proliferation, respectively (Fig. 5d). Immunofluorescence analysis further confirmed significantly upregulated VCL protein expression in the BPS group compared to the other groups, effectively promoting early cell adhesion (Fig. 5e). Overall, the multilayer design provided BPS composite membranes with superior biocompatibility, antibacterial performance, and active regulation of cell adhesion, demonstrating significant clinical potential.

3.6 Histological and immunohistochemical evaluation

To evaluate the repair capacity of BPS scaffolds, a rat full-thickness skin defect model was established for in vivo efficacy assessment (Fig. 6a). Given no significant differences between the PCL-h and PCL-a groups in vitro, three animal groups were established: untreated control, pure PCL membrane (PCL-p), and BPS. Macroscopic observations revealed scab formation and wound contraction initiation by day 4 (Figs. 6b and 6c). Undegraded materials were removed to clearly observe wound contraction trends, with the BPS group showing the most significant wound shrinkage. By day 7, all wounds showed considerable reduction with visible neo-skin tissue, and the BPS group maintained optimal repair efficacy. On day 14, the scaffold had fused with the skin tissue and mostly degraded. Macroscopic evaluation indicated significant repair across all groups, with BPS wounds almost completely healed and exhibiting the highest healing rate, confirming its intrinsic repair capacity based on its biocompatibility.

To assess skin regeneration processes, histological examinations were subsequently performed, including H&E staining, Masson's trichrome staining, CD31 immunofluorescence, and VCL immunohistochemistry (Fig. 6a). On day 4, all wounds were filled with granulation tissue rich in new capillaries (Yang et al., 2023). The BPS group exhibited significantly thicker granulation tissue than the control group (Fig. 6d), indicating advantages in early-stage repair. Collagen fiber remodeling, a critical step in wound healing (Doillon et al., 1985), began by day 7. Masson staining revealed that collagen deposition was approximately 1.6-fold higher in the BPS group than in the control group (Fig. 6g), with denser and more ordered fiber alignment, providing a foundation for

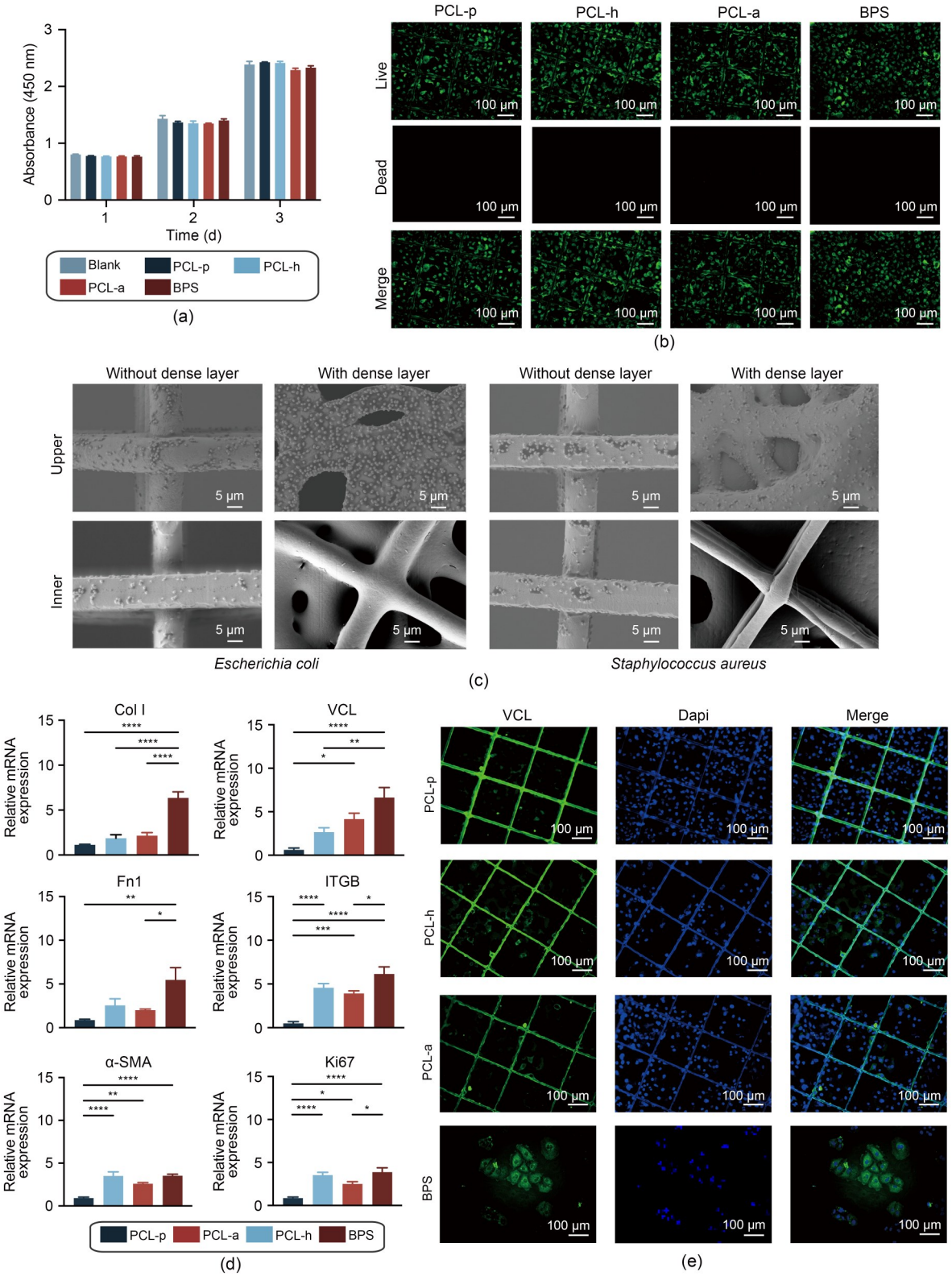

Fig. 5 Cellular and antimicrobial experiments for each group: (a) CCK-8 assay analysis of cell proliferation in each group on day 3; (b) live/dead cell staining images for each group; (c) antimicrobial SEM images of SL; (d) RT-PCR comparison graph (mean±SD, * P<0.05, ** P<0.01, *** P<0.001, **** P<0.0001, n=3); (e) immunofluorescence stained images for each group

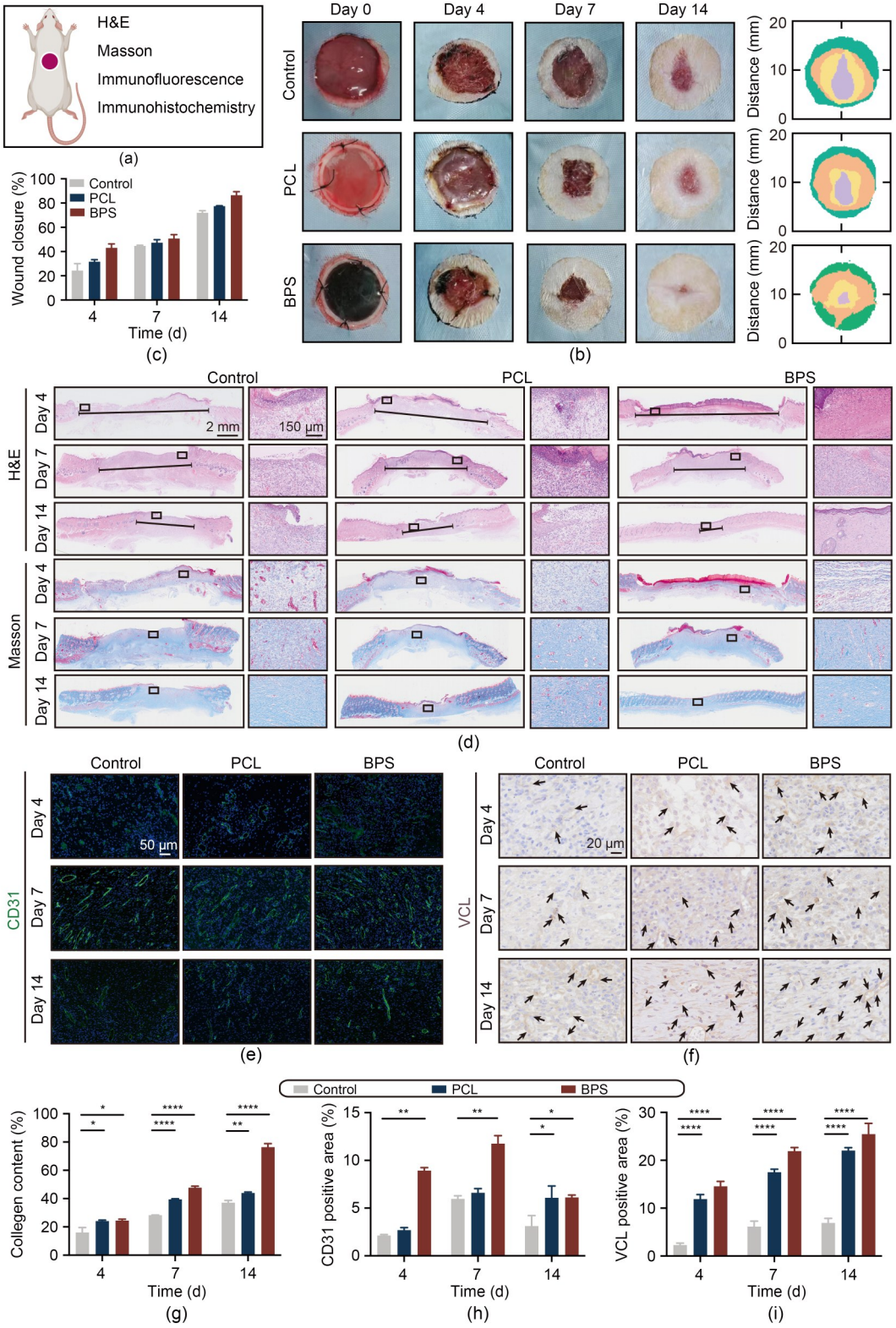

Fig. 6 In vivo evaluation of BPS for wound healing: (a) schematic diagram of rat full-thickness skin defect model; (b) gross images of wound healing in different groups on days 0, 4, 7, and 14; (c) comparison of wound healing rates; (d) H&E and Masson's trichrome staining on days 3, 7, and 14; (e) CD31 immunofluorescence staining; (f) VCL immunohistochemistry; (g) collagen content comparison; (h) CD31-positive cell count comparison; (i) VCL-positive cell count comparison (g–i: mean±SD, * P<0.05, ** P<0.01, **** P<0.0001, n=3)

subsequent structural reconstruction. By day 14, the BPS group achieved wound closure with intact neoepithelial tissue and epidermal thickness close to that of normal skin (Fig. 6d), attaining a wound closure rate of 92.5% (Fig. 6c) and demonstrating superior final repair outcomes. Wound healing and angiogenesis were evaluated by immunofluorescence and immunohistochemical analyses. On day 4, defect areas consisted mainly of capillary-rich granulation tissue. By day 7, maturing neovessels ensured oxygen and nutrient supply, reaching the maximum CD31-positive area. Day 14 showed nearly complete repair with reduced neovascularization. Notably, the BPS group showed the highest vascular density at all time points (Figs. 6e and 6h), indicating significant proangiogenic effects. Additionally, the BPS group exhibited peak VCL expression as early as day 4, indicating effective enhancement of cell adhesion by gelatin components. Throughout the repair process, the BPS group maintained persistently elevated VCL expression, gradually developing into mature tissue (Figs. 6f and 6i). Overall, the BPS scaffold improved the wound microenvironment by promoting angiogenesis, cell adhesion, and collagen deposition. Thus, it accelerated the transition from the inflammatory phase to the proliferative and maturation phases, optimizing the repair of full-thickness skin defects.

4 Conclusions

In this study, we successfully developed a wet-adhesive skin-repair ECM scaffold with a biomimetic multilayer structural design, effectively integrating biological function and mechanical property regulation. To address the limitations of traditional scaffolds in replicating the skin's multilayer dynamic barrier, an innovative epidermal-dermal-hypodermal bionic system was constructed: the SL achieves directional antibacterial and breathable functions through precisely regulated porous topology; the PL forms stable covalently crosslinked interfaces via chemical modification strategies, significantly enhancing interlayer mechanical transfer efficiency; the BL optimizes degradation using molecular chain reconstruction technology, precisely matching tissue regeneration cycles. Experimental validation confirmed that this biomimetic ECM scaffold exhibits excellent mechanical properties and biocompatibility, accelerating epithelialization in animal models. Its modular design overcomes the functional singularity of single-layer materials, achieving unified wound conformability, stability, and biological activity through synergistic effects of amino-active sites and dynamic crosslinking networks. This research provides a novel solution for complex wound repair. The structure–function coupled design can be extended to other tissue engineering applications, and integration with drug delivery systems holds promise for personalized precision therapy, offering transformative strategies in translational medicine.

Acknowledgments

This work is supported by the Huzhou Science and Technology Plan Project (No. 2023YZ42), the Zhejiang Provincial Key Research and Development Program (No. 2024C03081), and the Construction of Zhejiang Key Laboratory of Industrial Solid Waste Thermal Hydrolysis Technology and Intelligent Equipment (No. 2025ZY01056), China.

Author contributions

Kangning SHEN designed the research and wrote the first draft of the manuscript. Jingyi GU, Yinglin WANG, Yang SHI, and Kaiyang WANG performed the cellular and animal experiments and data analysis. Ximin YUAN, Nian LIU, Jiabin CAI, Xinghua YE, and Minghao YANG helped to analyze the results. Zhiyong MA and Zhijian XIE revised and edited the final version.

Conflict of interest

Kangning SHEN, Jingyi GU, Ximin YUAN, Nian LIU, Yinglin WANG, Jiabin CAI, Yang SHI, Kaiyang WANG, Xinghua YE, Minghao YANG, Zhiyong MA, and Zhijian XIE declare that they have no conflict of interest.

Ethical approval

The animal study was approved by the Ethics Committee for Animal Research at Zhejiang University (No. ZJU20250126).

References

Agrawal A, Rahbar N, Calvert PD, 2013. Strong fiber-reinforced hydrogel. *Acta Biomaterialia*, 9(2):5313-5318. https://doi.org/10.1016/j.actbio.2012.10.011

AQSIQ (General Administration of Quality Supervision, Inspection and Quarantine of the People's Republic of China), 2006. Plastics–Determination of Tensile Properties–Part 3: Test Conditions for Films and Sheets, GB/T 1040.3-2006. National Standards of the People's Republic of China (in Chinese).

Arif ZU, Khalid MY, Noroozi R, et al., 2022. Recent advances in 3D-printed polylactide and polycaprolactone-based biomaterials for tissue engineering applications. *International*

Journal of Biological Macromolecules, 218:930-968. https://doi.org/10.1016/j.ijbiomac.2022.07.140

ASTM (American Society for Testing and Materials), 2016. Standard Test Method for in vitro Degradation Testing of Hydrolytically Degradable Polymer Resins and Fabricated Forms for Surgical Implants, ASTM F1635-16. ASTM International, West Conshohocken, USA.

ASTM (American Society for Testing and Materials), 2024. Standard Test Method for Strength Properties of Tissue Adhesives in T-Peel by Tension Loading, ASTM F2256-24. ASTM International, West Conshohocken, USA.

Barbu A, Neamtu B, Zăhan M, et al., 2021. Current trends in advanced alginate-based wound dressings for chronic wounds. *Journal of Personalized Medicine*, 11(9):890. https://doi.org/10.3390/jpm11090890

Barros Almeida I, Garcez Barretto Teixeira L, Oliveira de Carvalho F, et al., 2021. Smart dressings for wound healing: a review. *Advances in Skin & Wound Care*, 34(2): 1-8. https://doi.org/10.1097/01.ASW.0000725188.95109.68

Boateng J, Catanzano O, 2015. Advanced therapeutic dressings for effective wound healing—a review. *Journal of Pharmaceutical Sciences*, 104(11):3653-3680. https://doi.org/10.1002/jps.24610

Brohem CA, da Silva Cardeal LB, Tiago M, et al., 2011. Artificial skin in perspective: concepts and applications. *Pigment Cell & Melanoma Research*, 24(1):35-50. https://doi.org/10.1111/j.1755-148X.2010.00786.x

Chen Y, Ma YZ, Fu JZ, et al., 2025. Design and fabrication of biomimetic four-region drug-loaded cartilage scaffolds with porous hollow fibers. *Journal of Zhejiang University-SCIENCE A*, 26(11):1070-1082. https://doi.org/10.1631/jzus.A2400513

Chen YW, Fu T, Zou ZF, et al., 2025. Biological reinforced concrete for cartilage repair with 3D printing. *Advanced Science*, 12(16):2416734. https://doi.org/10.1002/advs.202416734

Dhandayuthapani B, Yoshida Y, Maekawa T, et al., 2011. Polymeric scaffolds in tissue engineering application: a review. *International Journal of Polymer*, 2011:290602. https://doi.org/10.1155/2011/290602

Doillon CJ, Dunn MG, Bender E, et al., 1985. Collagen fiber formation in repair tissue: development of strength and toughness. *Collagen and Related Research*, 5(6):481-492. https://doi.org/10.1016/s0174-173x(85)80002-9

Drobnik J, Stebel A, 2017. Tangled history of the European uses of *Sphagnum* moss and sphagnol. *Journal of Ethnopharmacology*, 209:41-49. https://doi.org/10.1016/j.jep.2017.07.025

Gronbeck C, Feng H, 2023. Distribution of intermediate and complex skin repairs performed by dermatologists following updated 2020 coding guidelines. *Journal of the American Academy of Dermatology*, 88(4):954-956. https://doi.org/10.1016/j.jaad.2022.11.032

Guarino RD, Chaney BN, Liebmann-Vinson A, et al., 2007. Peptides for Enhanced Cell Attachment and Growth. US Patent 7157275.

Guo LZ, Zhang L, Wang ZM, et al., 2023. Direct construction of strong, tough, conductive, and adhesive hydrogel bioelectronics enabled by salt-dissolved cellulose. *Materials Today Communications*, 37:107002. https://doi.org/10.1016/j.mtcomm.2023.107002

Han L, Liu ZX, Li M, et al., 2025. 3D bioprinting of a dermal scaffold for full-thickness skin tissue regeneration. *Bio-Design and Manufacturing*, 8:68-84. https://doi.org/10.1631/bdm.2400058

Hunter-Featherstone E, Young N, Chamberlain K, et al., 2021. Culturing keratinocytes on biomimetic substrates facilitates improved epidermal assembly in vitro. *Cells*, 10(5): 1177. https://doi.org/10.3390/cells10051177

Huo XS, Wang JL, Cong ZH, et al., 2025. Strong and tough eutectogels with broad-range tunable mechanical properties via the hydrogen bond network-specific effect. *Advanced Functional Materials*, 35(27):2422464. https://doi.org/10.1002/adfm.202422464

Li XY, Gong JP, 2024. Design principles for strong and tough hydrogels. *Nature Reviews Materials*, 9(6):380-398. https://doi.org/10.1038/s41578-024-00672-3

Liu J, Wang SY, Xu K, et al., 2020. Fabrication of double crosslinked chitosan/gelatin membranes with Na^+ and pH dual-responsive controlled permeability. *Carbohydrate Polymers*, 236:115963. https://doi.org/10.1016/j.carbpol.2020.115963

Liu N, Shi Y, Li JY, et al., 2025. Morphology-guided cellular behavior modulation with 3D-printed engineered ECM. *Cell Biomaterials*, 1(6):100090. https://doi.org/10.1016/j.celbio.2025.100090

Maaz Arif M, Khan SM, Gull N, et al., 2021. Polymer-based biomaterials for chronic wound management: promises and challenges. *International Journal of Pharmaceutics*, 598:120270. https://doi.org/10.1016/j.ijpharm.2021.120270

Meng Q, Shen C, 2018. Construction of low contracted 3D skin equivalents by genipin cross-linking. *Experimental Dermatology*, 27(10):1098-1103. https://doi.org/10.1111/exd.13725

Nian GD, Kim J, Bao XY, et al., 2022. Making highly elastic and tough hydrogels from doughs. *Advanced Materials*, 34(50):2206577. https://doi.org/10.1002/adma.202206577

Obagi Z, Damiani G, Grada A, et al., 2019. Principles of wound dressings: a review. *Surgical Technology International*, 35:50-57.

O'Brien FJ, 2011. Biomaterials & scaffolds for tissue engineering. *Materials Today*, 14(3):88-95. https://doi.org/10.1016/S1369-7021(11)70058-X

Oomens CWJ, van Vijven M, Peters GWM, 2017. Skin mechanics. *In*: Payan Y, Ohayon J (Eds.), Biomechanics of Living Organs. Academic Press, London, UK, p.347-357. https://doi.org/10.1016/B978-0-12-804009-6.00016-X

Pan P, Hu C, Liang AH, et al., 2023. Preparation and properties of antibacterial silk fibroin scaffolds. *Polymers*, 15(23): 4581. https://doi.org/10.3390/polym15234581

Park J, Kim TY, Kim Y, et al., 2023. A mechanically resilient

and tissue-conformable hydrogel with hemostatic and antibacterial capabilities for wound care. *Advanced Science*, 10(30):2303651. https://doi.org/10.1002/advs.202303651

Patel AK, Michaud P, Petit E, et al., 2013. Development of a chitosan-based adhesive. Application to wood bonding. *Journal of Applied Polymer Science*, 127(6):5014-5021. https://doi.org/10.1002/app.38097

Peng W, Li D, Dai KL, et al., 2022. Recent progress of collagen, chitosan, alginate and other hydrogels in skin repair and wound dressing applications. *International Journal of Biological Macromolecules*, 208:400-408. https://doi.org/10.1016/j.ijbiomac.2022.03.002

Robinson TM, Hutmacher DW, Dalton PD, 2019. The next frontier in melt electrospinning: taming the jet. *Advanced Functional Materials*, 29(44):1904664. https://doi.org/10.1002/adfm.201904664

Singer AJ, Clark RAF, 1999. Cutaneous wound healing. *New England Journal of Medicine*, 341(10):738-746. https://doi.org/10.1056/NEJM199909023411006

Tang P, Song P, Peng ZY, et al., 2021. Chondrocyte-laden GelMA hydrogel combined with 3D printed PLA scaffolds for auricle regeneration. *Materials Science and Engineering: C*, 130:112423. https://doi.org/10.1016/j.msec.2021.112423

Trichet L, Le Digabel J, Hawkins RJ, et al., 2012. Evidence of a large-scale mechanosensing mechanism for cellular adaptation to substrate stiffness. *Proceedings of the National Academy of Sciences*, 109(18):6933-6938. https://doi.org/10.1073/pnas.1117810109

van den Bosch E, Gielens C, 2003. Gelatin degradation at elevated temperature. *International Journal of Biological Macromolecules*, 32(3-5):129-138. https://doi.org/10.1016/s0141-8130(03)00046-1

Wu SJ, Wu JJ, Kaser SJ, et al., 2024. A 3D printable tissue adhesive. *Nature Communications*, 15(1):1215. https://doi.org/10.1038/s41467-024-45147-9

Yang YT, Li M, Pan GY, et al., 2023. Multiple stimuli-responsive nanozyme-based cryogels with controlled NO release as self-adaptive wound dressing for infected wound healing. *Advanced Functional Materials*, 33(31):2214089. https://doi.org/10.1002/adfm.202214089

Yao K, Lv S, Zhang XJ, et al., 2025. 3D printing of multiscale biomimetic scaffold for tendon regeneration. *Advanced Functional Materials*, 35(4):2413970. https://doi.org/10.1002/adfm.202413970

Yazdi SJM, Baqersad J, 2022. Mechanical modeling and characterization of human skin: a review. *Journal of Biomechanics*, 130:110864. https://doi.org/10.1016/j.jbiomech.2021.110864

Yu YB, Xu S, Li SM, et al., 2021. Genipin-cross-linked hydrogels based on biomaterials for drug delivery: a review. *Biomaterials Science*, 9(5):1583-1597. https://doi.org/10.1039/d0bm01403f

Zhang L, Wang SH, Wang ZM, et al., 2023. A sweat-pH-enabled strongly adhesive hydrogel for self-powered e-skin applications. *Materials Horizons*, 10(6):2271-2280. https://doi.org/10.1039/d3mh00174a

Zhao WX, Hu CX, Wang YN, et al., 2025. Optimization-based conformal path planning for in situ bioprinting during complex skin defect repair. *Bio-Design and Manufacturing*, 8:1-19. https://doi.org/10.1631/bdm.2300365

Zhou Y, Zhuo RX, Liu ZL, 2005. Synthesis and characterization of novel aliphatic poly(carbonate-ester)s with functional pendent groups. *Macromolecular Rapid Communications*, 26(16):1309-1314. https://doi.org/10.1002/marc.200500222

Zussman E, Chaganti SR, Venugopal JR, et al., 2018. Fiber-Reinforced Hydrogel Composites and Methods of Forming Fiber-Reinforced Hydrogel Composites. US Patent 9950093.

Electronic supplementary materials

Figs. S1–S6; Table S1